Please provide feedback

Please support the ScholarWorks@UMBC repository by emailing scholarworks-group@umbc.edu and telling us what having access to this work means to you and why it's important to you. Thank you.

G359.13142-0.20005: A steep spectrum radio pulsar candidate with an X-ray counterpart running into the Galactic Center Snake (G359.1-0.2)

F. Yusef-Zadeh[1]★, Jun-Hui Zhao[2], R. Arendt[3], M. Wardle[4], C. O. Heinke[5], M. Royster[6], C. Lang[7], & J. Michail[1]

[1]*Department of Physics and Astronomy Northwestern University, Evanston, IL 60208*

[2]*Center for Astrophysics | Harvard-Smithsonian, 60 Garden Street, Cambridge, MA 02138, USA*

[3]*UMBC/GSFC/CRESST 2, Code 665, NASA/GSFC, 8800 Greenbelt Rd, Greenbelt MD 20771*

[4]*School of Mathematical and Physical Sciences, Centre for Astronomy and Space Technology, Macquarie University, Sydney NSW 2109, Australia*

[5]*Department of Physics, CCIS 4-183, University of Alberta, Edmonton, AB T6G 2E1, Canada*

[6]*Department of Physics, College of the Sequoias, CA, 93277, USA*

[7]*Department of Physics and Astronomy, University of Iowa, Iowa City, IA, 52242, USA*

ABSTRACT

The Snake is a remarkable Galactic center radio filament with a morphology characterized by two kinks along its $\sim 20'$ extent. The major and minor kinks are located where the filament is most distorted from a linear magnetized structure running perpendicular to the Galactic plane. We present *Chandra*, VLA, and MeerKAT data and report the detection of an X-ray and radio source at the location of the major kink. High-resolution radio images of the major kink reveal a compact source with a steep spectrum with spectral index $\alpha \sim -2.7$ surrounded by extended emission. The radio luminosity and steep spectrum of the compact source are consistent with a pulsar. We also show flattening of the spectrum and enhanced synchrotron emissivity away from the position of the major kink along the Snake, which suggests injection of relativistic particles along the Snake. We argue that the major kink is created by a fast-moving ($\sim 500 - 1000$ km s^{-1}), object punching into the Snake, distorting its magnetic structure, and producing X-ray emission. X-ray emission pinpoints an active acceleration site where the interaction is taking place. A secondary kink is argued to be induced by the impact of the high-velocity object producing the major kink.

Key words: cosmic rays: Interstellar Medium - ISM: magnetic fields - stars: pulsars - Galaxy: centre

1 INTRODUCTION

It has been close to 40 years since the discovery of the nonthermal radio filaments (NRFs) associated with the Radio Arc in the Galactic Center (Yusef-Zadeh, Morris & Chance 1984). NRFs with similar characteristics have been discovered in the intervening years with a range of morphology. Recently, radio continuum MeerKAT images of the inner $3.5° × 2.5°$ of the Galactic center at 20 cm revealed an order of magnitude increase in their number (Heywood, et al. 2019). NRFs appear as single filaments or groups of parallel filaments with mean angular spacing $\sim 16''$ (Yusef-Zadeh et al. 2022a). The mean spectral index of all the filaments ($\alpha \sim -0.83$, where $\alpha = d(\log F_\nu)/d(\log \nu)$, is steeper than that of supernova remnants (SNRs; $\alpha = -0.62$). The equipartition magnetic field strengths along the filaments range from ~ 100 to 0.4 mG depending on the assumed ratio of cosmic-ray protons to electrons. NRFs run mainly perpendicular to the Galactic plane. The intrinsic polarization observed from these filaments shows that their internal magnetic fields are directed along the filaments (Yusef-Zadeh et al. 1997; Paré et al. 2019). The mechanisms responsible for accelerating particles to relativistic energies and for creating the elongated filamentary geometry are still mysterious. Some authors have examined how the filaments might arise from their interaction with molecular and ionized clouds or with mass-losing stars (Rosner & Bodo 1996; Shore & LaRosa 1999; Bicknell & Li 2001; Yusef-Zadeh & Wardle 2019). Although numerous other models have been proposed to explain the origin of the filaments, there is no consensus how these filaments are produced (Nicholls & Le Strange 1995; Rosner & Bodo 1996; Shore & LaRosa 1999; Bicknell & Li 2001; Dahlburg et al. 2002; Yusef-Zadeh 2003; Boldyrev & Yusef-Zadeh 2006; Ferrière 2009; Yusef-Zadeh & Wardle 2019; Thomas, Pfrommer & Enßlin 2020; Sofue 2020; Coughlin et al. 2021; Gopal-Krishna & Biermann 2024). Broadly speaking nonthermal filament (NTF) models invoke either a single energetic event at the Galactic center, a compact source accelerating cosmic rays to high energies, or a process that involves the turbulent environment of the Galactic center hosting a high cosmic-ray flux. A similar mystery to the origin of the filaments is the recent discovery of long structures in radio galaxies (Rudnick et al. 2022). Recent comparison of the populations of magnetized filaments in the Galactic center and radio galaxies in

★ E-mail: zadeh@northwestern.edu
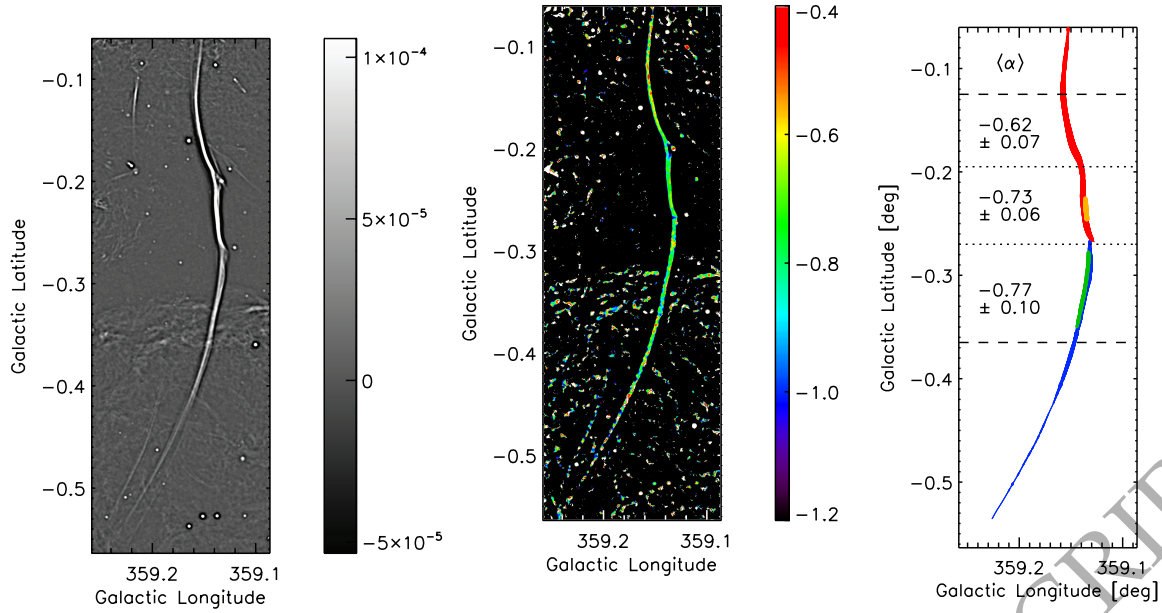
Figure 1. *(Left, a)* A filtered image of the the total intensity of the Snake at 1.28 GHz with 6.4″ resolution (Yusef-Zadeh et al. 2022a) based on MeerKAT observations (Heywood et al. 2022). The unit in the grey scale bar is Jansky beam^{-1}. *(Middle, b)* The in-band spectral index at 1.28 GHz (20cm or L band) values along the Snake stretched to values between -0.83 and -0.31. The colors are used as key to identify the 4 sub-filaments (see Fig. 2). The spectral index in the color scale bar ranges between -1.2 and -0.4. *(Right, c)* Color traces of different sub-filaments in the Snake. The colors are arbitrarily chosen to distinguish the four sub-filaments. The mean spectral indices within three bright intervals of the Snake are listed (and shown in more detail in Figure 2). The uncertainties on $< \alpha >$ are the standard deviation of α for each segment.

the intercluster medium (ICM) suggests that that they are analogous to each other as might be anticipated based on their similar morphologies, in spite of vastly different physical properties, such as lengths, widths and magnetic field strengths (Yusef-Zadeh et al. 2022b).

The Snake is one of the longest, ∼ 30′ (∼ 70 pc), brightest, and most spectacular filaments in the Galactic center distinguishing itself by the presence of two kinks along its length (Gray, et al. 1991, 1995). H 1 absorption line studies imply that the Snake is located at the 8 kpc distance of the Galactic center (Uchida et al. 1992). This filament is narrow (< 10″ or < 0.4 pc in width) and runs perpendicular to the Galactic plane (Heywood, et al. 2019). Like numerous other filaments in the Galactic center, the Snake shows no obvious external powering source. Most Galactic center filaments exhibit smooth curvature, but the Snake shows two distorted kinks, north (major kink) and south (minor kink), and three different curvatures along its length (Gray, et al. 1995; Yusef-Zadeh et al. 2022a). It was also reported that two compact radio sources, G359.132-0.200 and G359.120-0.265, are located to the west of the major and minor kinks, respectively. The equipartition magnetic field of the Snake is strongest, ∼ 0.15 mG, to its north as it decreases to its south (Yusef-Zadeh et al. 2022a). Faraday rotation measures (RMs) of 5500 and 1400 rad m^{-2} have been reported to be due to an external and internal medium, respectively (Gray, et al. 1995).

Chandra, XMM and NuStar have detected X-ray emission from a handful of radio filaments with X-ray spectral indices consistent with synchrotron emission. The X-ray spectral index and normalization is consistent with a broken power-law spectrum (Sakano, et al. 2003; Lu, Wang & Lang 2003; Yusef-Zadeh, et al. 2005; Zhang, et al. 2014; Ponti et al. 2015; Yusef-Zadeh et al. 2021). Here we report the detection of X-ray emission from a source adjacent to the Snake, near the location of the major kink. There is a compact radio counterpart to the X-ray source at 6 and 1.2 GHz with a steep spectrum. Both radio and X-ray emission appear to show extended structure pointing in the direction of the Snake. We suggest a picture in which the major and minor kinks are created, likely by a fast-moving pulsar, running into the Snake, and distorting the magnetic structure of the Snake. This interaction picture is supported by the following measurements: a spectral change in the radio along the filament, a change in the morphology, and X-ray emission.

2 OBSERVATIONS

2.1 Radio VLA data

2.1.1 X-band (wide) data

As part of a targeted survey of the central few degrees of the Galactic center, six overlapping fields were observed toward the Snake using the VLA X-band (wide) receiver at 10 GHz in the C-array configuration on July 31 and August 16, 2021. The correlator was configured for 64 channels in each of 32 sub-bands with a channel width of 2 MHz, producing producing all four Stokes parameters (RR, RL, LR and LL) with a total bandwidth of 4 GHz covering a frequency range from 8 to 12 GHz. 3C 286, NRAO 530 and J1744-3116 were interleaved in the the
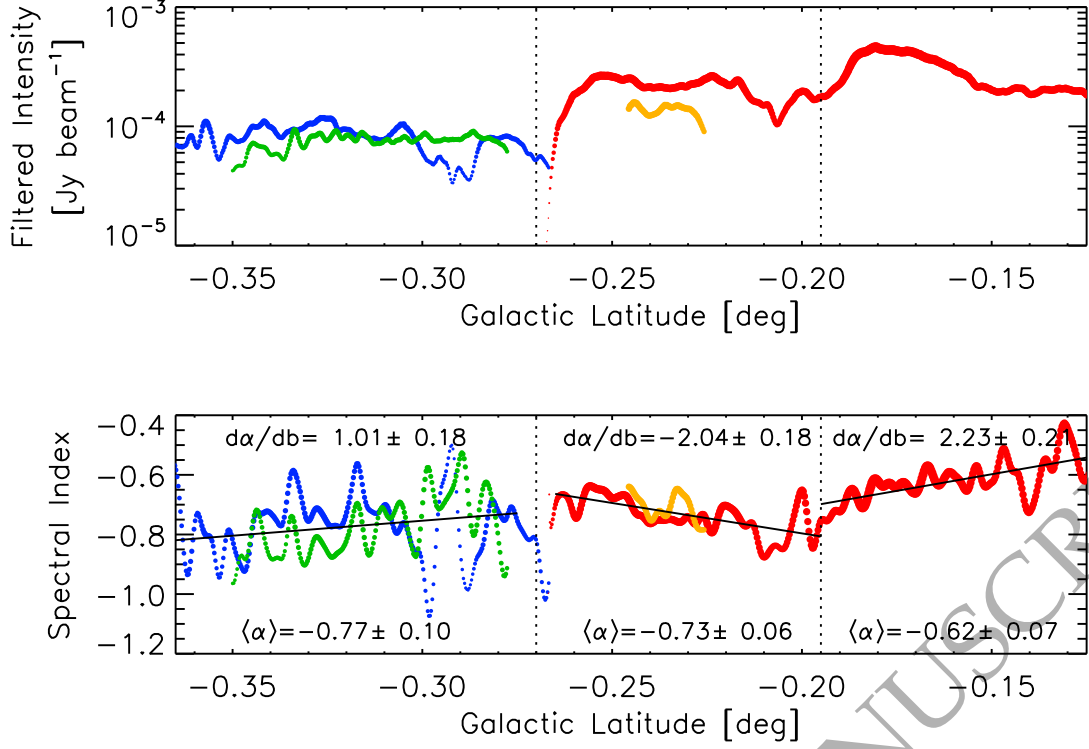
Figure 2. *(Top a)* The values of the total intensity as a function of latitude along a slice cut along the four segments shown in the right panel of Figure 1 with a 4″ × 4″ beam. *(Bottom, b)* Similar to the left panel, the mean spectral index values and gradients with their uncertainties as a function of latitude at 1.28 GHz with an 8′ × 8″′ beam. The uncertainties are derived from fitting the slopes. Color coding corresponds to different pieces of sub-filaments, as shown in right panels of Figure 1.

survey observing runs for calibrations of complex gains, bandpass, and flux density scales. The initial calibrations were carried out using a VLA pipeline program. The residual corrections were further conducted using a model of J1744-3116 including both the core and extended structure. Table 1 summarizes the observations of the six mosaic fields and lists the images produced from the observations of the Snake. Polarization analysis of the Snake, providing the intrinsic direction of the magnetic field and the rotation measure distribution, will be given elsewhere.

Total intensity images are constructed using CASA (The CASA Team et al. 2022) task *tClean* with gridding options of mosaic, utilizing the multi-frequency synthesis (MFS) algorithm for the first Taylor expansion term (tt0) with $R = 0.6$ for robustness visibility weighting (Briggs 1995). The sidelobes were cleaned with the Multi-term MFS algorithm (Conway, Cornwell & Wilkinson 1990; Rau & Cornwell 2011), *mtmfs*, a deconvolution option in tClean of CASA. The rms noise is 4 μJy beam^{-1} and FWHM = 4.0″ × 3.5″ (PA= −14°, the angle of the major axis of the beam, measured east of north in celestial coordinates). To determine the flux densities of the compact radio sources in the vicinity of the Snake at 10 GHz, with less contamination from the extended emission, we imaged two pointing fields taken in the C-array configuration survey at X-band, X2F16 and X2F19, with $R = -0.6$ and a filter rejecting the shorter baseline visibility data. The two images (X2F16.I.R-0.6.tt0 and X2F19.I.R-0.6.tt0) were convolved to a beam of 3.2″ × 1.6″ (PA= −14°).

2.1.2 L-band data

The Snake was also observed with the VLA on March 6, and 8, 2021 in the A-array configuration with a correlator setup configuring 128 channels in each of 12 subbands with channel width of 1 MHz for RR, RL, LR and LL correlations. A data calibration procedure similar to that for the X-band data was followed concerning pipeline reduction and residual-error corrections.

Other archival VLA observations were also obtained toward Sgr C centered at (J2000 17^{h}44^{m}35^s.0, −29°29′ 00″.0) having a field of view that included the Snake. These A-array measurements were carried out at L-band (1–2 GHz) on August 20, 2015. The initial flagging and reference calibration was performed using the VLA casa pipeline8 and processed with the wsclean multi-scale clean algorithm with a resolution of ~ 1″ × 2.5″. Further details on the use of the VLA data can be found in Heywood et al. (2022).

Table 1. Log of VLA X-band uv datasets

Field ID	Array	Band	ν (GHz)	$\Delta\nu$ (GHz)	Δt (sec)	Obs. time (min)	Epoch (date)
(1)	(2)	(3)	(4)	(5)	(6)	(7)	(8)
Project-ID: 21A-000							
F04: G359.12-0.27	C	X[†]	10	4	3	23	July 31, 2021
F15: G359.12-0.27	C	X	10	4	3	23	August 16, 2021
F16: G359.13-0.20	C	X	10	4	3	23	August 16, 2021
F17: G359.21-0.10	C	X	10	4	3	23	August 16, 2021
F18: G359.22-0.14	C	X	10	4	3	23	August 16, 2021
F19: G359.22-0.19	C	X	10	4	3	23	August 16, 2021

For UV data – (1) The poining ID of the survey fields. (2) The VLA array configuration code. C array corresponds to the maximum baseline of 3 km. (3) The VLA band code; "X" stand for the VLA bands in the ranges of 8 – 12 GHz (https://science.nrao.edu/facilities/vla/docs/manuals/oss2013B/performance/bands). (4) The observing frequencies at the observing band center. (5) The total bandwidth. (6) The integration time. (7) The total on-source observing time. (8) The observing date.
[†]Correlator setup: 64 channels in each of 32 subbands with channel width of 2 MHz for RR, RL, LR, LL.

2.1.3 C-band data

The Snake was also observed at 6 GHz in the VLA A-array configuration on July 12, 2020 with a wideband correlator setup similar to the X-band survey described in Table 1, i.e., with 64 channels in each of 32 sub-bands with a channel width of 2 MHz for RR, RL, LR, LL correlations. The C-band data were initially calibrated using a VLA pipeline program. The residual errors were corrected using the J1744-03116 data and a non-point source model developed following the procedure described in (Zhao, Morris, & Goss 2019).

The effective total bandwidth of 4 GHz was used, centered at 6 GHz. By synthesizing a 4 GHz bandwidth of the wideband spectral data, we made a high resolution image with a robustness parameter of 0 for visibility weighting (Briggs 1995) to have a FWHM beam of $0.69'' \times 0.28''$. A compact radio source G359.13142-0.20005 was detected with a flux density 0.20 ± 0.01 mJy at 6 GHz, located near the X-ray source. In order to determine the spectrum of the compact radio source, a continuum spectral image cube was constructed by averaging every four sub-band data sequentially along the frequency axis. Then, the sidelobes of the image cube were cleaned with the mtmfs algorithm in tClean of CASA. Thus, in addition to the 4-GHz bandwidth synthesized image at 6 GHz, we have eight more spectral images at 4.23, 4.74, 5.35, 5.76, 6.23, 6.74, 7.25, and 7.76 GHz across the C band. A range of rms from 0.014 to 0.025 mJy beam^{-1} was achieved for the C-band spectral images.

2.2 Radio MeerKAT data

Details of MeerKAT L-band observations, mosaicking of multiple fields and in-band spectral index measurements based on unfiltered and filtered images are found in Heywood, et al. (2019); Heywood et al. (2022); Yusef-Zadeh et al. (2022a). Briefly, the L-band (856−1712 MHz) centered at 1.28 GHz system was used, with the correlator configured to deliver 4,096 frequency channels, which were averaged by a factor of 4 prior to processing and was imaged with an angular resolution of $4''$. The MeerKAT image was spatially filtered to remove large scale backgrounds (Yusef-Zadeh et al. 2022a). Point sources in the filtered image correspond to the spatial resolution having FWHM ∼ $6.4''$. An in-band spectral index mosaic was produced with a resolution of $8'' \times 8''$. The in-band spectral index is determined using cubes of 16 filtered frequency channels. To improve the signal-to-noise ratio (S/N), the median spectral index of each filament is determined from the median of the pixel spectral indices along its length. The statistical uncertainty of the mean spectral index is typically ∼ 0.1, but can drop as low as 0.01 for long bright filaments.

2.3 X-ray data

The Snake's major kink is covered by archival Chandra ACIS-I ObsIDs 658, 2278, 2286, 18332, and 18645; and by archival Chandra HRC-I ObsID 2714. We retrieve the level=2 event files from the Chandra Data Archive. We merge these ACIS-I observations using the CIAO reproject-obs command, and restrict the energy range for the output image to 2-8 keV. X-ray analysis of these images are discussed in §3.2.1.
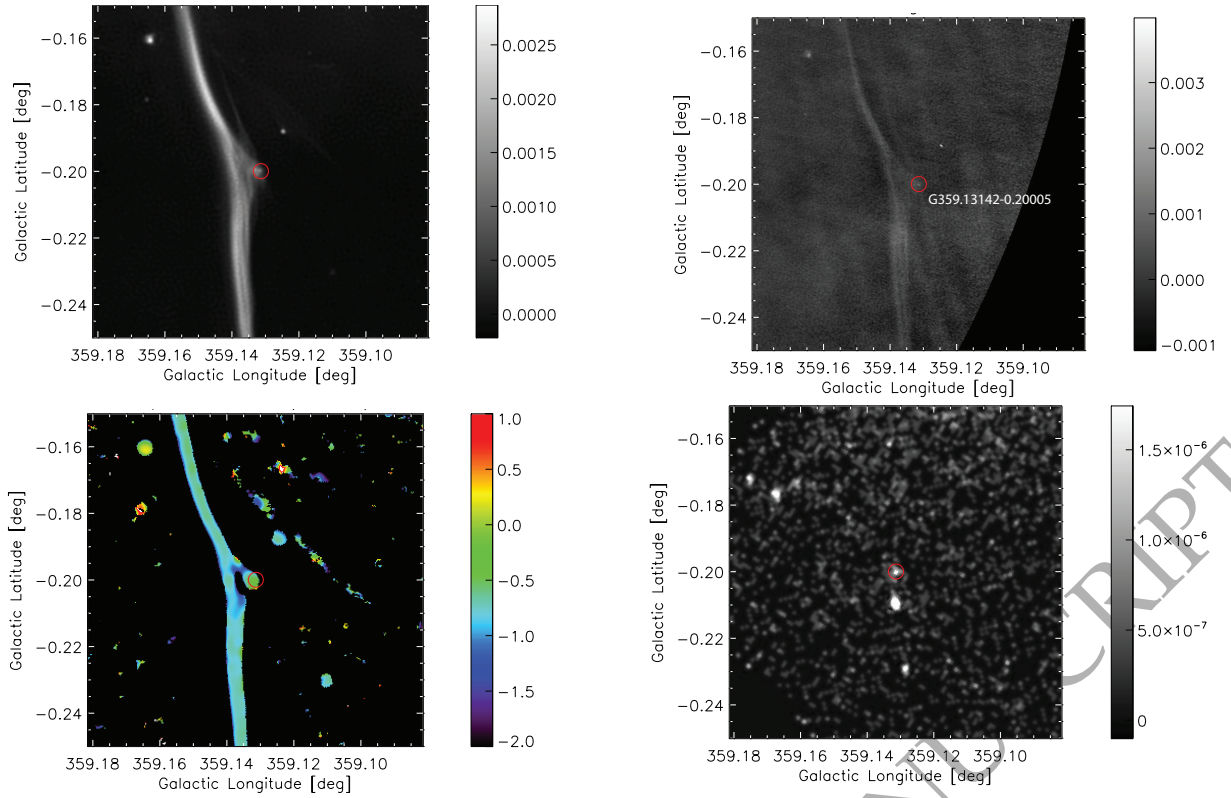
Figure 3. (Top Left, a), An unfiltered MeerKAT image of the major kink of the Snake with a 4″ spatial resolution at 1.28 GHz (Heywood et al. 2022). (Top Right, b) Similar to (a) except a VLA image with a spatial resolution of 6.9″ × 2.78″ (PA=169°) at 1.52 GHz. (Bottom Left, c) Similar to the left panel except the spectral index distribution with a spatial resolution of ∼ 8″ (Heywood et al. 2022; Yusef-Zadeh et al. 2022a). (Bottom Right, d) An X-ray 2-8 keV image based on Chandra observations convolved with a 2D Gaussian 4″. The gray scale bar units in (a) and (b) are Jy beam^{-1}, (c) shows the spectral index values, and in (d) counts s^{-1} cm^{-2}. Red circles show the location of the compact radio source G359.13142-0.20005.

3 RESULTS

We first describe the spectral index distribution along the Snake followed by morphological details of the kinks. Properties of X-ray emission from a source located at the western tip of the major kink will also be described.

3.1 Intensity and Spectral index distributions

Figure 1, left shows details of the intensity distribution of the Snake with the major and minor kinks, at Galactic latitudes $b \sim -0.2°$ and $\sim -0.27°$ respectively, that show similar morphology. The kinks split the Snake into three segments. The north and middle segments are bows to the (Galactic) east with a tighter radius of curvature than the south segment which bows to the west. The top two segments are brighter than the south segment by roughly a factor of two. There are also sub-filaments in the Snake, defined as parallel strands of filaments. The main filament of the Snake (top segment) breaks up into multiple sub-filaments at the location G359.14-0.19, with brightness reduced by a factor of 1.5 at 20 cm, thus suggesting that the Snake is disturbed in this region. The equipartition magnetic field of the north segment is reported to be high, reaching 0.15 mG field (Yusef-Zadeh et al. 2022a). We notice that the Snake consists of bundles of filaments with small spacings. Figure 1, middle illustrates the spectral index along the Snake. Figure 1, right shows a better color representation, distinguishing the four sub-filaments that are plotted in Figure 2. The sub-filaments are selected because they are spatially distinct in brightness and not because of their spectral index (see also Figure 6, left where two sub-filaments, north and south of $\sim -0.27°$, correspond to the red/orange, and green/blue pairs in Figures 1, right and 2).

The mean spectral index values for each segment of the Snake indicates steepening of the mean spectral index from -0.62 to -0.73 in the direction to the south of the major kink. The mean spectral index is $\sum \alpha(b)/N_b$, where $\alpha(b)$ is the spectral index at each pixel (at latitude b), and N_b is the total number of pixels summed. The gradients are change in the spectral index per degree latitude ($degree^{-1}$). The regions in the direction away from the northern kink show enhanced synchrotron emissivity with a spectrum that becomes steeper to a value of ~ -0.8 at the southern end. This suggests that cosmic ray particles are more recently accelerated to the north of the major kink, than to the south of the minor kink.

Figure 2 (top and bottom) shows details of the variation of the intensity and spectral index as a function of latitude using filtered images of the Snake at 1.28 GHz. A slice is cut along the individual segments of the intensity and the spectral index images of the Snake. The spectral
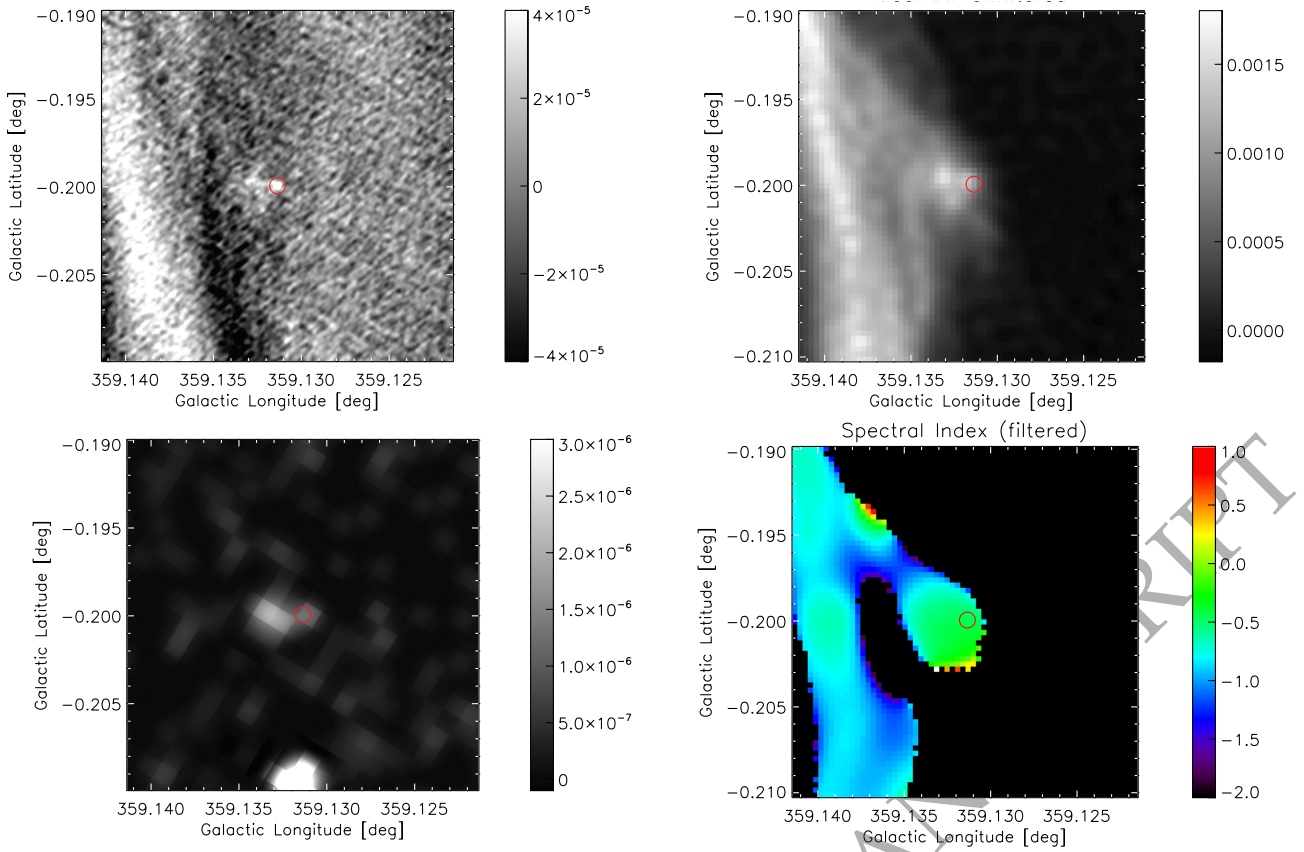
Figure 4. *(Top Left, a)* A 6 GHz VLA image of the major kink reveals the appearance of a bow-shock morphology with a compact source and diffuse emission behind it with a resolution~ $1'' \times 0.8''$. *(Top Right, b)* Same as (a) except the total intensity image of the major kink at 1.28 GHz with a resolution of $4''$. *(Bottom Left, c)* An X-ray counterpart to the radio sources appears to consist of two components coincident with the compact radio source and its extended liner morphology. *(Bottom Right, d)* The spectral index of the major kink shows a mixture of steep and flat spectral at 20cm. The grayscale bars units in (a), and (b) are in Jy beam^{-1} and (c) is in counts s^{-1} cm^{-2}.

index gradients displayed as black lines indicate flattening of the spectral index away from the major kink, away from $\sim b = -0.19°$, (dotted vertical line). A mixture of flatter extended non-thermal emission along the Snake and a steeper emission from particles injected at the major kink is likely to explain the unusual spectral gradient.

The linear segment to the south of the minor kink near $\sim b = -0.27°$, as shown in Figure 2 bottom, shows steepening of the mean spectral index $\alpha = -0.77$. The overall mean spectral index distribution of the Snake indicates steepening with decreasing latitudes. The Snake's minor kink also shows a spectral index gradient in which the filaments become steeper away from the minor kink, opposite to that seen in the major kink. This suggests that the origin of the major kink may be different than the minor kink.

3.2 Major kink G359.13-0.20

Figures 3 (top left, top right) show close-up views of the $6' \times 6'$ region of the major kink at 1.28 and 1.52 GHz based on MeerKAT and VLA observations. A red circle shows the location where a compact radio source G359.13142-0.20005 is noted to the west of the filaments. The spectral index of this source is discussed below. We note distorted structure of the filaments, diffuse emission connecting the compact source to the major kink, as well as multiple parallel sub-filaments, with a separation of $\sim 7''$, to the south of the major kink. In addition, Figure 3 (bottom left) shows a close-up view of the spectral index image of the major kink with a spatial resolution of $8''$ indicating that the compact source surrounded by an extended diffuse emission has a flatter spectrum $\alpha \sim -0.3$ than the rest of the filaments. Altogether, these morphological and spectral characteristics suggest an interaction at the location of the major kink.
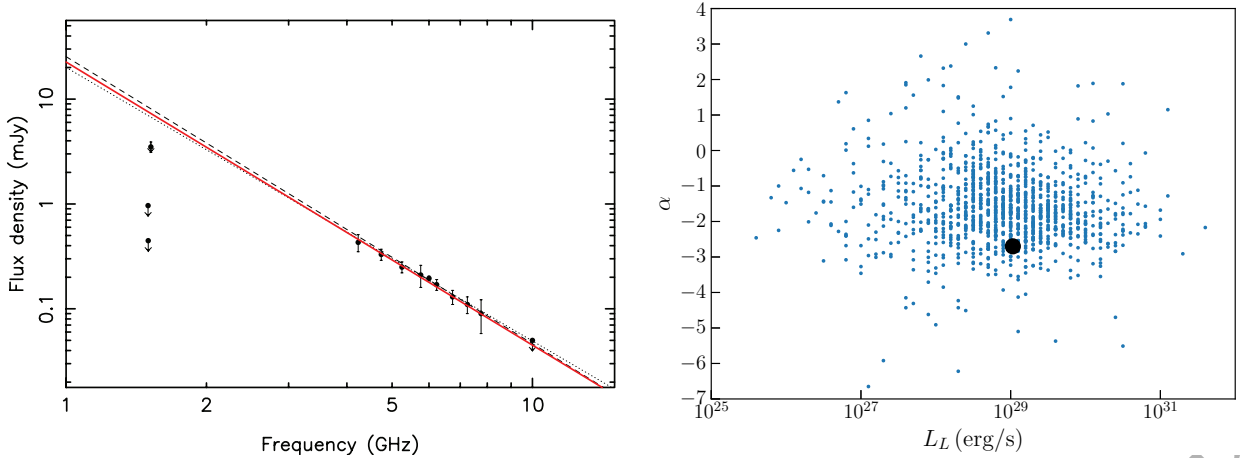
Figure 5. *(Left, a)* The spectrum of the compact source in the major kink G359.13142-0.20005 gives a spectral index $\alpha = -2.7$. The spectrum is fitted by a power-law $F_\nu \propto \nu^\alpha$ for C-band data only (dashed line) and all data (dotted line) listed in Table 2, respectively. We derived α and σ_α from a least-squares fitting weighted by the inverse variance of the measurements, as discussed in the text. The red line on the spectrum plot shows the best fitted slope. *(Right, b)* Blue points show the spectral index and L-band pseudo-luminosity for pulsars in the Thousand Pulsar Array program (Posselt et al. 2023). The black point indicates the spectral index and L-band luminosity of the Snake compact source.

3.2.1 X-ray analysis

Using a merged image (from the CIAO *reproject-obs* command) of the ACIS-I exposures in the 2-8 keV band (totaling 36.3 ks), we used *wavdetect* to find the J2000 (Galactic) coordinates of two sources: $17^h44^m21^s57$, $-29°47'10''0$, hereafter "southern source", (G359.1316-0.20160), and $17^h44^m19^s22$, $-29°46'53''4$, " northern source", (G359.13142-0.20005). The southern source is clearly detected in the HRC-I image and in ACIS images below 2 keV (indicating a foreground source), while the northern source is only detected above 2 keV, consistent with a Galactic Bulge distance. The northern Chandra source has no counterparts within 1'' in a Vizier search except for Chandra source identifications in the Chandra Source Catalog (Evans et al. 2010; Muno et al. 2009; Wang et al. 2016). The southern source is consistent (within 0.2'', smaller than the typical Chandra ACIS uncertainty of 0.8'') with Gaia source4056860326361166848, G=19.6, geometric parallax distance estimate of 800^{+300}_{-200} pc (Bailer-Jones et al. 2021). We do not consider the southern source further.

The northern X-ray source matches the position of a compact steep spectrum radio source within the 0.8'' Chandra astrometric accuracy[1]. There is a hint of extended emission from this X-ray source, though it is not formally detected by wavdetect. In the combined X-ray image, as shown in Figure 3 (bottom right), the point source has 13±4 counts according to *wavdetect*, while the extended emission, pointing to the east (Galactic coordinates, see Fig. 4 bottom left) of the compact X-ray source has about 40 counts.

We extracted spectra from both the point source and the extended emission, using a circle of radius 2.5'' for the point source and a box of sides 8.8'' × 12.7'', from the three longer ObsIDs which contained more than one photon from each source (2278, 2286, and 658). We bin the spectra by 1 photon/bin, and fit the spectra simultaneously in XSPEC using the W-statistic (Cash 1979) with an absorbed power-law model (using wilm abundances, (Wilms, Allen, & McCray 2000)). We then fit the point source with the normalization, spectral index, and hydrogen column density N_H free. However, the parameters are very poorly constrained, and tend toward rather high values of both N_H (2×10^{23} cm^{-2}) and spectral index (4), which we find somewhat unlikely. We thus try fits with one parameter fixed at a plausible value. If N_H is fixed at 6×10^{22} cm^{-2}, then the power-law photon index is $1.1^{+1.1}_{-1.1}$. If the power-law photon index is fixed at 2.0, then N_H is $1.2^{+1.0}_{-0.6} \times 10^{23}$ cm^{-2}. The unabsorbed 2-10 keV flux is 6.6×10^{-14} erg s^{-1} cm^{-2}, or 8.3×10^{-14}, for these two models.

We followed the same process with the spectral fitting of the extended emission. Again the parameters are very poorly constrained when all three parameters are free. If N_H is fixed at 6×10^{22} cm^{-2}, then the power-law photon index is -0.1 ± 1.1. If the power-law photon index is fixed at 2.0, then $N_H = 2^{+2}_{-1} \times 10^{23}$ cm^{-2}. The unabsorbed 2-10 keV flux is roughly 1×10^{-13} erg s^{-1} cm^{-2} for either scenario.

A close view of the radio counterpart to the X-ray source at 6 and 1.28 GHz are displayed in Figures 4 (top left, top right), respectively. The high-resolution ($\sim 1'' \times 0.8''$) VLA image of the $\sim 1'$ region of the major kink (Fig. 1 top left) shows a compact radio source with an elongated tail-like structure to its east. A Gaussian fit to the compact radio source G359.13142-0.20005 at 6 GHz (Epoch date December 12, 2020) gives J2000 coordinates $17^h 44^m 19^s2444 \pm 0.0013$, $-29° 46' 52''9651 \pm 0.0323$ with a spatial resolution of $0''72 \times 0''32$ (PA=170°.92). Figure 4 (top right) displays the MeerKAT image of the same region with a resolution of $4'' \times 4''$ and illustrates that the compact radio/X-ray sources are embedded within the diffuse and distorted region of the major kink. Figure 4 (bottom left) shows a faint X-ray source which appears to coincide with the tail of the compact radio source shown in Figure 4 (top left). We note that both the radio and X-ray sources are extended,

---

[1] https://cxc.harvard.edu/cal/ASPECT/celmon/
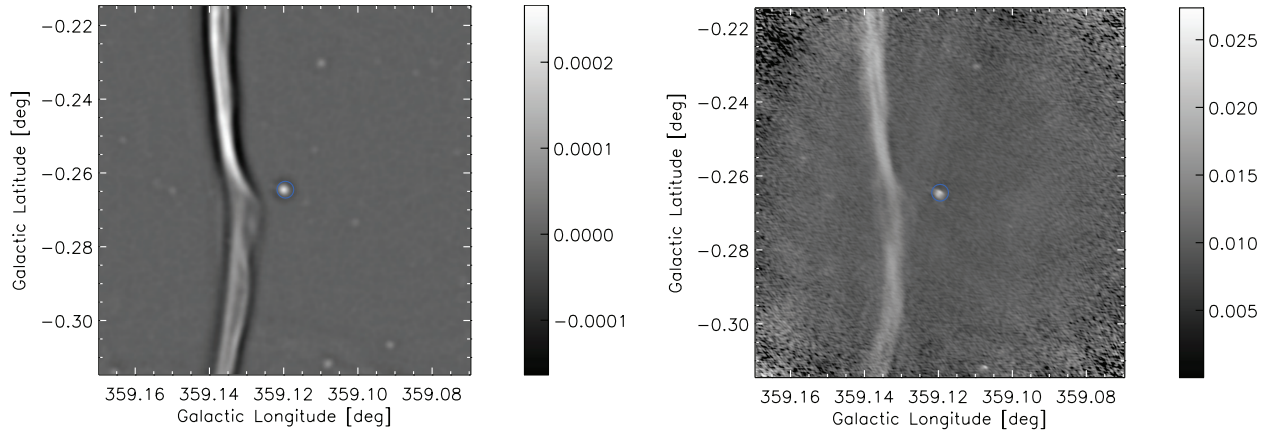
Figure 6. *(Left, a)* A close-up view of the minor kink is based on a filtered image of the the total intensity at 1.28 GHz with 6.4″ resolution (Yusef-Zadeh et al. 2022a) based on MeerKAT observations. *(Right, b)* Similar to Figure 3 (top right) except close-up view of the minor kink based on a VLA image with a resolution 6.9″ × 2.78″ (PA=169°) at 1.52 GHz. This image is not primary beam corrected. The color bars units in (a) and (b) are in Jansky beam^{-1}. The blue circle corresponds to the position of the radio source G359.120-0.265.

Table 2. The compact radio source at 6 and 10 GHz in the major kink♣

ID	RA(J2000) Dec(J2000)	$S_{6\text{GHz}} \pm \sigma_S$ (mJy)	$S_{10\text{GHz}} \pm \sigma_S$ (mJy)	$\alpha \pm \sigma_\alpha$
(1)	(2)	(3)	(4)	(5)
G359.13142-0.20005	17:44:19.244 −29:46:52.96	0.20±0.01	< 0.05	−2.70 ± 0.05

♣Column (1) is the source ID with their Galactic coordinates, column (2) is the equatorial coordinates at Epoch J2000, with uncertainty of $\sigma_\theta = 0.5\theta(F_{6\text{GHz}}/\sigma_F)$, roughly 0.02" or less. Column (3) and (4) the flux densities with 1σ uncertainties. For the non-detections, 3σ upper limits are inferred. Column (5) the spectral index derived from least square fitting (see text). The errors are derived from the largest range of the 1σ uncertainties.

with a head-tail morphology. Figure 4 (bottom right) shows a close-up view of the in-band spectral index of the compact and extended radio emission with a resolution of $\sim 8″ \times 8″$ at 1.28 GHz using unfiltered image cube (Yusef-Zadeh et al. 2022a). The spectral index varies between 0 and -0.6.

3.2.2 The compact source in the major kink G359.13142-0.20005

To determine the nature of the compact radio source in the major kink, we used the wideband VLA C-band (6 GHz), L-band (1.5 GHz) and X-band (10 GHz) data sets. With a 2D gaussian model, we fitted the compact radio source in both the wideband (4GHz-BW) synthesized image at 6 GHz and the 8 spectral images (0.5GHz-BW) of the image cube to determine the flux densities at the central frequencies of the sub-bands in C band from 4.23 to 7.76 GHz. The least-squares fitting the flux-density measurements simultaneously observed in C-band on December 7, 2020 to a power-law spectrum is shown in Figure 5, left (the dashed straight line) with $\alpha = -2.74 \pm 0.05$.

The X-band image was synthesized 4-GHz bandwidth data with a baseline cutoff (> 20 kilo wavelengths) to filter out the contamination from diffuse emission sampled in shorter baseline data providing a sensitive image with an rms of 0.015 mJy beam^{-1}. The compact radio source was not detected at 10 GHz on August 16, 2021, placing a 3-sigma upper limit of 0.05 mJy in flux density.

The L-band data at three different epochs, separated in 2 days in 2021 which spans > 5 year from the 2015 observations. The source of 3.5 ± 0.4 mJy was detected significantly from the 2015 observation while at both epochs in the 2021 VLA A-array survey, the source was not detected, giving 3-sigma upper limits of 0.9 and 0.5 mJy on March 6 and 8, 2021, respectively. The VLA high-resolution observations at X-band, C-band and L-band suggest G359.13142 - 0.20005 is variable (either due to intrinsic or interstellar scintillation)

We note that for those flux density values measured from non-PB corrected images, a PB correction factor A(x) was determined from polynomial parameters given by (Perley 2016). The corresponding uncertainty is calculated using the equation (2) of (Zhao, Morris, & Goss 2020). Including all the X-band, C-band and L-band data with an inverse-variance weighting, a slightly shallow spectrum of $\alpha = -2.61 \pm 0.04$ is derived. Thus, hereafter, we take a mean value of $\alpha = -2.7$ as the spectral index of the compact radio source. The radio properties of G359.13142-0.20005 are summarized in Table 2.
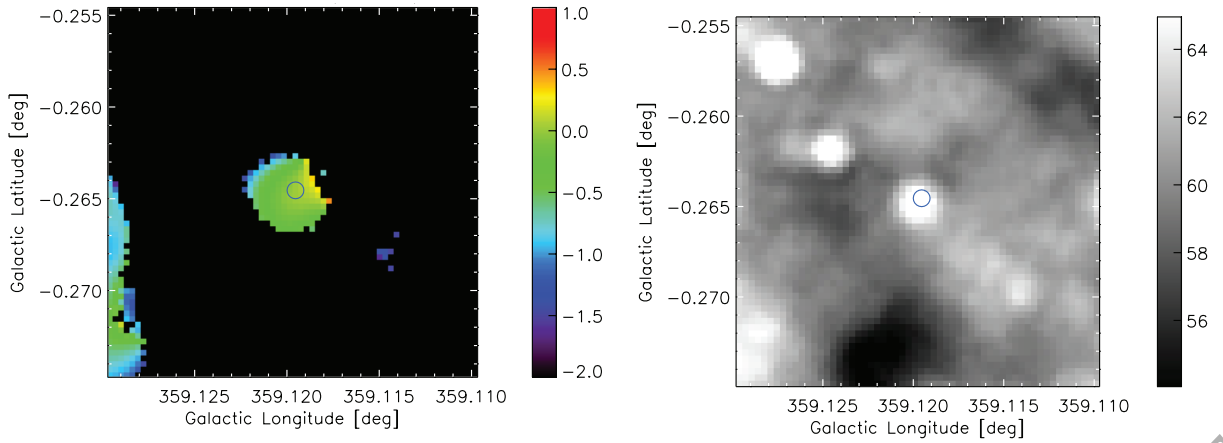
Figure 7. *(Left, a)* An in-band spectral index map of the radio source G359.120-0.265 based on filtered MeerKAT images at 20cm shows a spectral index near zero (Heywood et al. 2022; Yusef-Zadeh et al. 2022a). *(Right, b)* A 24μm infrared counterpart to G359.120-0.265 revealing thermal nature of the source. Blue circles in (a) and (b) show the location of G359.120-0.265. The color bar unit in (b) is in MJy sr^{-1}.

3.2.3 The compact radio source, a pulsar candidate

The steep radio spectrum ($\nu^{-2.7}$) of the compact source is suggestive of a pulsar, and the radio luminosity is consistent with this hypothesis. The estimated L-band radio luminosity is $4\pi d^2 \nu S_\nu \approx 1.1 \times 10^{29}$ erg s^{-1} for $\nu = 1.2$ GHz, $S_\nu = 1$ mJy and a distance $d = 8$ kpc. In Figure 5, right, we show a scatter plot of L-band spectral index against pseudo-luminosity of the 1200 pulsars in the Thousand Pulsar Array program (Posselt et al. 2023). The spectral index and luminosity of the G359.13142-0.20005 are marked by a black filled circle in Figure 5, right, and are consistent with the general pulsar population.

3.3 Minor kink G359.13-0.27

Another rendition of the MeerKAT image at 1.28 GHz shows a close-up view of the minor kink in Figure 6, left. We note bright sub-filaments to the north and south of the minor kink giving the appearance of twisted magnetized filaments. Figure 6, right shows a higher resolution VLA image revealing faint diffuse emission surrounding the minor kink. The apparent twisting of the sub-filaments is also seen in this image. Morphologically, the apparent twisting of the filaments, sub-filamentation and the presence of diffuse emission surrounding the kink are likely distorted by an external influence. The variation of the mean spectral index from $< \alpha > = -0.73$ to -0.77 as well as the mean spectral index gradient from $d\alpha/db = -1.98$ to 1.0 deg^{-1} provides another support for the suggestion that there is disturbance at the position of the minor kink.

Similar to the the major kink, another candidate radio source G359.120-0.265 could be responsible for producing the minor kink. This radio source G359.12-0.265 lies to the west of the Snake, as circled in Figure 6. Figure 7 shows the spectral index image of the compact source as well as its 24 μm infrared counterpart identified in *Spitzer* data. The flat spectral index close to -0.11 and the presence of 24μm dust emission are consistent with a thermal source, possible an HII region. This suggests that G359.120-0.265 is unlikely to be associated with the minor kink.

4 DISCUSSION

The most interesting result of our study is that the Snake exhibits several signatures of an interaction at the location of the major kink: (i) the distortion of the Snake from a straight geometry, unlike nearly all other filaments that show a smooth curvature; (ii) sub-filamentation at the kinks where the Snake is most distorted; (iii) an increase in the radio surface brightness away from the major kink; (iv) spectral index variation and flattening of the spectrum of the electrons away from the major kink; (v) the presence of an X-ray source coincident with the major kink as well as an extended tail at both radio and X-rays suggesting a bow-shock morphology.

We suggest a scenario in which the major and minor kinks in the Snake result from the collision of a fast-moving nonthermal source (possibly a runaway pulsar) that punches through an otherwise smooth curved magnetic structure associated with a pre-existing Galactic center filament. Figure 8 shows a schematic diagram of this scenario where two cusps representing major and minor kinks. If the interaction of the fast-moving object is sufficiently strong, the magnetized filament is pulled to one side (to the west of the vertical filament), creating the major kink and sending disturbances propagating along the filament in opposite directions. If the interaction is sufficiently violent, the disturbance propagates as a kink-like shock. We identify the minor kink as the current location of such a shock propagating southwards from the interaction point, i.e. from the major kink. We also note multiple sub-filaments at the location of the minor kink, tracing the disturbance to the south. There is, however, no corresponding minor kink to the north, presumably because the natural signal speed of the magnetized filament there
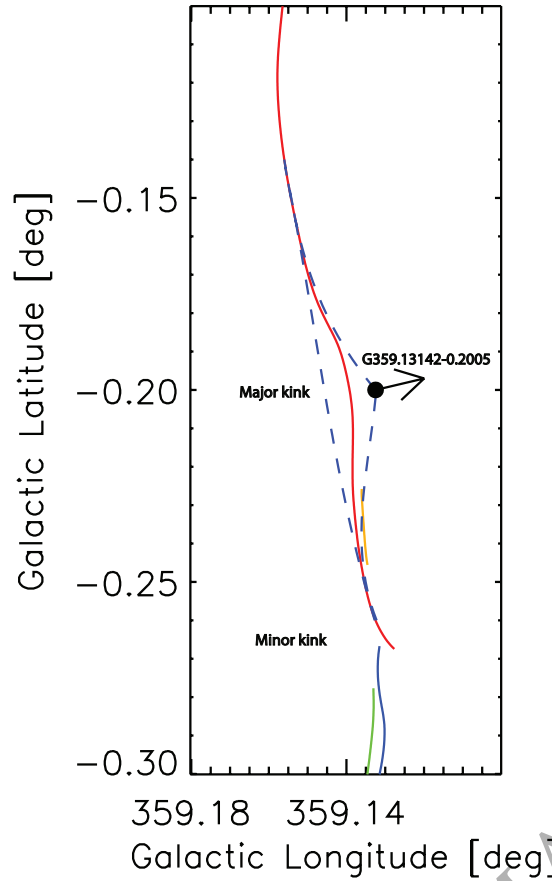
Figure 8. A schematic diagram of an object (black circle) running into the Snake and distorting the shape of a straight filament. Four sub-filaments are traced showing both kinks. Additional interpolations, blue dashed lines, are also drawn.

is significantly faster than to the south. In this case the disturbance propagates along the filament as a smooth transverse wave traveling at the filament's signal speed. This picture is supported by the observation that the brightest segment of the Snake lies to the north of the major kink and likely has a significantly higher magnetic field than the segment to the south.

We have already suggested that the steep-spectrum and radio luminosity of the compact radio source are consistent with the time-averaged pulsed emission of a pulsar. The extended radio emission visible at 6 and 1.4 GHz has a head-tail structure, and its orientation is consistent with the motion required by the interaction scenario above. This likely synchrotron emission from electrons accelerated in a shock created by the interaction of a pulsar wind nebula (PWN) with the local interstellar medium, or from oppositely-directed jets of electron-positron pairs emerging from the poles of the pulsar and swept back by its motion through the surroundings.

We now consider the X-ray emission, which although faint and relatively poorly resolved, is consistent with a head-tail structure. One possibility is that this is also synchrotron radiation from energetic electrons and positrons directly accelerated by the pulsar. In support of this, we note that the compact and extended X-ray components that we detect have similar unabsorbed fluxes between 2 and 10 keV, $F_x \approx 1 \times 10^{-13}$ erg cm^{-2} s^{-1}. At 8 kpc this yields X-ray luminosity $L_x \approx 8 \times 10^{32}$ erg s^{-1}, in the center of the 10^{29}–10^{37} erg s^{-1} range of known PWN and their associated pulsars (see, e.g. Table 1 and Fig. 1 of Hsiang & Chang 2021).

5 SUMMARY

We presented the spectral index and morphological details of one of the most prominent nonthermal radio filaments, the Snake, in the Galactic center. Radio observations revealed a steep spectrum radio source at the location where the Snake is most distorted, known as the major kink. The steep radio spectrum ($\nu^{-2.7}$) of the compact source is suggestive of a fast-moving object ($\sim 500 - 1000$ km s^{-1}), likely a pulsar, that is interacting with the Snake. In this picture, the fast-moving object drags material from the Snake, with a trail behind it and is expected to be connected to the filament by diffuse emission behind the compact source. To examine the interaction hypothesis, we analyzed archival Chandra data which reveal a weak X-ray source at the location of the major kink. Alternatively, a secondary source may be responsible for disturbing the minor kink, independent of the the pulsar candidate. A thermal source lies to the west of the Snake, and there is no extended emission between the thermal source and the Snake. The physical picture of the pulsar wind nebula candidate and the vertical nonthermal filaments of the Snake resembles other filamentary structures in the Galactic enter. Two examples are the nonthermal compact radio and X-ray source

G0.13-0.11 lying along a nonthermal filament of the Radio Arc (Churazov et al. 2023) and the compact radio source in the network of Harp filaments (Thomas, Pfrommer & Enßlin 2020; Heywood et al. 2022; Yusef-Zadeh et al. 2022a). It is possible that a PWN injecting synchrotron emitting electrons into spatially intermittent magnetic field flux tubes (Thomas, Pfrommer & Enßlin 2020) could explain the origin of these filaments including the Snake.

Future sensitive and high-resolution imaging at radio and X-rays including proper motion measurements will examine the interaction picture that we described here. These measurements provide insights on the origin of one of most remarkable radio filaments in the Galactic center

6 DATA AVAILABILITY

All the data including MeerKAT that we used here are available online and are not proprietary. We have reduced and calibrated these data and these are available if requested.

REFERENCES

Alexander T., 2012, EPJWC, 5001, EPJWC..39

Alves, M. I. R., Calabretta, M., Davies, R. D., et al. 2015, MNRAS, 450, 2025

Bailer-Jones C. A. L., Rybizki J., Fouesneau M., Demleitner M., Andrae R., 2021, AJ, 161, 147. doi:10.3847/1538-3881/abd806

Bicknell G. V., Li J., 2001, ApJ, 548, L69

Boldyrev, S. & Yusef-Zadeh, F. 2006, ApJ, 637, L101

Briggs, Daniel S. 1995, PhD Dissertation, High Fidelity Deconvolution of Moderately Resolved Sources, New Mexico Institute of Mining and Technology, https://casa.nrao.edu/Documents/Briggs-PhD.pdf

The CASA Team et al 2022, PASP, 134, 114501

Cash W., 1979, ApJ, 228, 939. doi:10.1086/156922

Churazov E., Khabibullin I., Barnouin T., Bucciantini N., Costa E., Di Gesu L., Di Marco A., et al., 2023, arXiv, arXiv:2312.04421. doi:10.48550/arXiv.2312.04421

Clark, B. G. 1980, A&A, 89, 377

Conway, J. E., Cornwell, T. J. & Wilkinson, P. N. 1990, MNRAS, 246, 490

Coughlin, E. R., Nixon, C. J., & Ginsburg, A. 2021, MNRAS, 501, 1868

Dahlburg, R. B., Einaudi, G., LaRosa, T. N., et al. 2002, ApJ, 568, 220

Evans I. N., Primini F. A., Glotfelty K. J., Anderson C. S., Bonaventura N. R., Chen J. C., Davis J. E., et al., 2010, ApJS, 189, 37. doi:10.1088/0067-0049/189/1/37

Ferrière, K. 2009, AA, 505, 1183.

Gray A. D., Cram L. E., Ekers R. D., Goss W. M., 1991, Nature, 353, 237

Gray A. D., Nicholls J., Ekers R. D., Cram L. E., 1995, ApJ, 448, 164

Gopal-Krishna, Biermann P. L., 2024, MNRAS, 529, L135. doi:10.1093/mnrasl/slad191

Heywood I., et al., 2019, Natur, 573, 235

Heywood I., Rammala I., Camilo F., Cotton W. D., Yusef-Zadeh F., Abbott T. D., Adam R. M., et al., 2022, ApJ, 925, 165. doi:10.3847/1538-4357/ac449a

Högbom J. A. 1974, A&A, 15, 417

Hsiang J.-Y., Chang H.-K., 2021, MNRAS, 502, 390. doi:10.1093/mnras/stab025

Johnson S. P., Dong H., Wang Q. D., 2009, MNRAS, 399, 1429

LaRosa T. N., Nord M. E., Lazio T. J. W., Kassim N. E., 2004, ApJ, 607, 302

Law C. J., Yusef-Zadeh F., Cotton W. D., 2008, ApJS, 177, 515

Leahy, J. P., Jägers,W. J. & Pooley, G. G. 1986, A&A, 156, 234

Liszt H. S., 1985, ApJ, 293, L65

Lu F. J., Wang Q. D., Lang C. C., 2003, AJ, 126, 319

Muno M. P., Bauer F. E., Baganoff F. K., Bandyopadhyay R. M., Bower G. C., Brandt W. N., Broos P. S., et al., 2009, ApJS, 181, 110. doi:10.1088/0067-0049/181/1/110

Nicholls, J. & Le Strange, E. T. 1995, ApJ, 443, 638.

Paré, D. M., Lang, C. C., Morris, M. R., et al. 2019, ApJ, 884, 170

Perley, R. 2016, NRAO EVLA Memo 195

Ponti G., Morris M. R., Terrier R., Haberl F., Sturm R., Clavel M., Soldi S., et al., 2015, MNRAS, 453, 172. doi:10.1093/mnras/stv1331

Posselt B., Karastergiou A., Johnston S., Parthasarathy A., Oswald L. S., Main R. A., Basu A., et al., 2023, MNRAS, 520, 4582. doi:10.1093/mnras/stac3383

Rau, U. & Conwell, T. J. 2011,AA, 532, A71

Rudnick L., Bruggen M., Brunetti G., Cotton W., Forman W., Jones T. W., Nolting C., et al., 2022, arXiv, arXiv:2206.14319

Rosner R., Bodo G., 1996, ApJ, 470, L49

Sakano M., Warwick R. S., Decourchelle A., Predehl P., 2003, MNRAS, 340, 747

Shore S. N., LaRosa T. N., 1999, ApJ, 521, 587

Sofue, Y. 2020, PASJ, 72, L4

Thomas T., Pfrommer C., Enßlin T., 2020, ApJL, 890, L18

Uchida, K., Morris, M., Bally, J., Pound, M. and Yusef-Zadeh, F., 1992, ApJ, 398, 128.

Wang S., Liu J., Qiu Y., Bai Y., Yang H., Guo J., Zhang P., 2016, ApJS, 224, 40. doi:10.3847/0067-0049/224/2/40

Wilms J., Allen A., McCray R., 2000, ApJ, 542, 914. doi:10.1086/317016

Yusef-Zadeh F., Morris M., Chance D., 1984, Nature, 310, 557

Yusef-Zadeh F., Wardle M., Muno M., Law C., Pound M., 2005, AdSpR, 35, 1074

Yusef-Zadeh F., Wardle M., 2019, MNRAS, 490, L1

Yusef-Zadeh, F., Wardle, M., & Parastaran, P. 1997, ApJ, 475, L119

Yusef-Zadeh F., Wardle M., Heinke C., Heywood I., Arendt R., Royster M., Cotton W., et al., 2021, MNRAS, 500, 3142. doi:10.1093/mnras/staa3257

Yusef-Zadeh, F. 2003, ApJ, 598, 325. doi:10.1086/378715

Yusef-Zadeh F., Arendt R. G., Wardle M., Heywood I., Cotton W., Camilo F., 2022,ApJL, 925, L18. doi:10.3847/2041-8213/ac4802

Yusef-Zadeh F., Arendt R. G., Wardle M., Heywood I., Cotton W., 2022, MNRAS, 517, 294. doi:10.1093/mnras/stac2415

Zhang S., et al., 2014, ApJ, 784, 6

Zhao J.-H., Morris M. R., Goss W. M., 2019, ApJ, 875, 134. doi:10.3847/1538-4357/ab11c4

Zhao, Jun-Hui, et al. 2024, in preparation

Zhao J.-H., Morris M. R., Goss W. M., 2020, ApJ, 905, 173. doi:10.3847/1538-4357/abc75e